DOI: 10.1002/ ((please add manuscript number))

**Article type: Review**

# Electron sandwich doubles the thermoelectric power factor of $SrTiO_3$

*Yuqiao Zhang and Hiromichi Ohta**

Y. Zhang, Prof. H. Ohta

Graduate School of Information Science and Technology, Hokkaido University, N14W9, Kita, Sapporo 060−0814, Japan

Prof. H. Ohta

Research Institute for Electronic Science, Hokkaido University, N20W10, Kita, Sapporo 001−0020, Japan

E-mail: hiromichi.ohta@es.hokudai.ac.jp

Keywords: thermoelectric power factor, de Broglie wavelength, superlattice, two-dimensionality, $SrTiO_3$−$SrNbO_3$ solid-solution

**Abstract**

Thermoelectric materials convert a temperature difference into electricity through a phenomenon known as the Seebeck effect, and their efficiency is determined by the dimensionless figure of merit, $ZT$ ($\equiv S^2 \cdot \sigma \cdot \kappa^{-1}$). Currently, most materials exhibiting high $ZT$ values ($ZT > 1$) are based on heavy metal compounds, but these materials have low thermal/chemical stability. In this regard, conducting metal oxides attract much attention for thermoelectric power generations at high temperatures on the basis of their advantages in

thermal stability over heavy metal compounds. However, the thermoelectric performance of metal oxides is usually low. Here we review that an enhanced two-dimensionality is efficient for enhancing the thermoelectric power factor of metal oxides. We fabricated $SrTiO_3$-based superlattices of [*N* unit cell $SrTi_{1-x}Nb_xO_3$|11 unit cell $SrTiO_3$]$_{10}$, of which the de Broglie wavelengths can be tuned by the substitution of Nb. The maximum power factor of the superlattice composed of the long de Broglie wavelength $SrTi_{1-x}Nb_xO_3$ exceeded ~5 mW $m^{-1}$ $K^{-2}$, which doubles the value observed from the optimized bulk $SrTi_{1-x}Nb_xO_3$. This finding could help reduce the amount of wasted heat and thus wasted fossil fuel in daily activities and industrial factories.

## 1. Introduction

### 1.1. Thermoelectrics

Recently, approximately 60 % of the energy is disposed in form of waste heat, deepening energy crisis as well as global warming. Hence, thermoelectric technology can offer an environmentally friendly solution to these issues since they allow a direct conversion between heat and electricity.[1, 2] In 1821, Thomas Johann Seebeck first discovered that a voltage is generated between the two ends of a metal bar when the bar exhibited a temperature difference[3], which is not known as the Seebeck effect. On the other hand, electric currents can also be used to modulate the flow of heat. For example, heating or cooling of metallic junctions occurs when electric currents flow through the system. This phenomenon was discovered by Jean Charles Athanase Peltier in 1834, which is now called the Peltier effect.

The performance of thermoelectric materials is evaluated by the dimensionless figure of merit, $ZT = S^2 \cdot \sigma \cdot T \cdot \kappa^{-1}$, where $Z$ is a figure of merit, $T$ is absolute temperature, $S$ is thermopower (≡ Seebeck coefficient), $\sigma$ is electrical conductivity and $\kappa$ is thermal conductivity. In order to

achieve high *ZT*, thermoelectric materials should simultaneously exhibit high *S*, $\sigma$ and low $\kappa$. The |*S*| of a thermoelectric material can be expressed by the Mott equation[4]:

$$S = \frac{\pi^2}{3}\frac{{k_B}^2 T}{e}\left\{\frac{d[\ln(\sigma(E))]}{dE}\right\}_{E=E_F} = \frac{\pi^2}{3}\frac{{k_B}^2 T}{e}\left\{\frac{1}{n}\cdot\frac{dn(E)}{dE} + \frac{1}{\mu}\cdot\frac{d\mu(E)}{dE}\right\}_{E=E_F}$$

, where $k_B$, *e*, *n*, and $\mu$ are the Boltzmann constant, electron charge, carrier concentration, and carrier mobility, respectively. Because of this relationship, trade-off relationships between *S* and $\sigma$ are commonly observed: $\sigma$ increases almost linearly with increasing *n*, while |*S*| decreases with *n*. Therefore, the value of $S^2\cdot\sigma$ (≡ power factor, PF) must be maximized by the means of *n*. In additon, the *ZT* also depends on $\kappa$, which is usually comprised of two major components: the electron thermal conductivity ($\kappa_{ele}$) and lattice thermal conductivity ($\kappa_{lat}$). $\kappa_{ele}$ can be estimated using $\sigma$ and the Wiedemann-Franz law[5],

$$\kappa_{ele} = L\cdot\sigma\cdot T = L\cdot n\cdot e\cdot\mu\cdot T$$

where *L* is the Lorenz number. $\kappa_{ele}$ is also dependent on *n*, and $\kappa_{lat}$ is the only factor that does not strongly depend on *n*. For these reasons, maximizing the PF while minimizing $\kappa$ can be very challenging.

The *ZT* of practical thermoelectric materials such as $Bi_2Te_3$ and PbTe are ≈1, which is currently believed to be the standard requirement for practical applications.[6, 7] Many high-performance thermoelectric materials have been proposed to date.[7-15] However, most of the waste heat at large scales (i.e. factories) is generated at very high temperatures (~700 °C). These extreme conditions are not suitable for heavy metal compounds like $Bi_2Te_3$ and PbTe due to their low thermal stability. Furthermore, heavy metal elements in these materials can also raise safety concerns such as toxicity and pollution.

### 1.2. Oxide thermoelectrics

As the demand for environmentally friendly thermoelectric materials is high, conducting metal oxides have been recieving a lot of attention for thermoelectric power generation at high temperatures due to their excellent thermal robustness [16-18]. During 1950's and 1970's, the pioneering researches were conducted on the thermoelectric properties of simple conducting oxides such as CdO[19], NiO[20], ZnO[21], $In_2O_3$[22], $SrTiO_3$[23], rutile-$TiO_2$[24], $SnO_2$[25], $Cu_2O$[26] and $Fe_3O_4$[27]. In 1986, the discovery of cuprous oxide based high $T_c$ superconducting oxides lead to studies on the thermoelectric properties of superconducting oxides, including $La_2CuO_4$[28], La-Ba-Cu-O[29], $YBa_2Cu_3O_{7-\delta}$[30] and Tl-Ca-Ba-Cu-O[31]. Most recently, the discovery of $CaMnO_3$[32], Al-doped ZnO[33], $Na_xCoO_2$[34], $Ca_3Co_4O_9$[35, 36] and $SrTiO_3$[37-41] further promoted researches on thermoelectric oxides. These materials are regarded as the most promising oxides for replacing their heavy metal based counterparts.

In case of p-type thermoelectric oxides, layered cobaltites are considered to be the one of the most promising candidates[34, 42]. Due to the low spin state of $Co^{3+}$, these materials shows very high thermopower[43]. These materials have layered crystal structures. $CoO_2$ plane provides a path for p-type charge carriers while the interfacial layers effectively scatter phonons and reduce the $\kappa_{lat}$. This type of materials demonstrates a good example of "phonon-glass, electron-crystal" in thermoelectric materials design[44]. The highest *ZT* achieved in these materials are 0.15−0.5 at 1000 K for $Ca_3Co_4O_9$ and 0.3−0.9 at 950 K for $Na_xCoO_2$.

$CaMnO_3$ is one of the most famous transition metal oxides for its special electrical and magnetic properties[45-48]. It is an n-type semiconductor which could be doped at either *A* sites or *B* sites. In 1995, Ohtaki *et al*. reported its high temperature thermoelectric performance with different dopings at *A* sites[32]. Ytterbium doping could also increase its electrical conductivity and thermopower[49, 50], and co-doping with dysprosium was shown to be very

effective for $\sigma$ enhancements as well as $\kappa$ reduction. The optimal $ZT$ obtained to date is 0.1−0.2 at 1000 K, which makes $CaMnO_3$ a good candidate for high temperature applications.

ZnO is another promising oxide thermoelectric material at high temperature. ZnO is a wide bandgap semiconductor, and therefore requires adequate doping to become a thermoelectric material. The dopants are usually n-type, and aluminum is the most widely adopted doping element. In addition to injecting conduction electrons, Al doping also refines the grains and introduces grain boundaries, which suppresses the $\kappa$. Oher dopants such as nickel, titanium, tin and antimony, are also used to modulate electron and phonon transports in ZnO[51-54]. At 1073 K, the optimized $ZT$ of ZnO is 0.5.

$SrTiO_3$ is known for its special behaviors in superconductivity and ferroelectricity. It is also on of the most famous single crystal substrates for epitaxial growth of other materials with similar lattice structures. Examples of such materials include $SrRuO_3$, $LaAlO_3$, FeSe, and more. Pure $SrTiO_3$ (space group $Pm\bar{3}m$, cubic perovskite structure, $a$ = 3.905 Å ) is a band insulator with a bandgap of 3.2 eV, of which the conduction band edge is composed of triply degenerate, empty Ti 3d-$t_{2g}$ orbitals, while the valence band edge is composed of fully occupied O 2p orbitals[55]. The $\sigma$ of $SrTiO_3$ can be easily controlled from insulator to metal by the substitutional doping of $La^{3+}$ ($A$ site) or $Nb^{5+}$ ($B$ site).

In 2001, Okuda *et al*. reported large PF from (2.8–3.6 mW $m^{-1}$ $K^{-2}$) $Sr_{1-x}La_xTiO_3$ ($0 \leq x \leq 0.1$) single crystals fabricated by floating-zone method[37]. Afterwards, Ohta *et al*. clarified thermoelectric transport properties of Nb- and La-doped $SrTiO_3$ single crystals ($n_e$ ~$10^{20}$ $cm^{-3}$) at high temperatures (~1000 K)[38], which indicated that the $ZT$ could be further improved by heavy Nb doping. However, due to the solubility limit of $Nb^{5+}$ in $SrTiO_3$, second phase formation is difficult to avoid, and it is very challenging to clarify the PF enhancement

at high doping levels. To resolve this issue, Ohta *et al*. grew epitaxial films of Nb-substituted $SrTiO_3$ to further increase Nb doping to achieve $n_e$ ~$2 \times 10^{21}$ $cm^{-3}$ and got an enhanced *ZT* of 0.37 at 1000 K[39]. In 2016, Lu *et al*.[40] successfully fabricated $SrTiO_3$-based ceramics with higher *ZT* (~0.4 at 973 K), which were sintered in a reducing atmosphere ($Sr_{1-3x/2}La_xTiO_{3-\delta}$). Moreover, Wang *et al*.[41] improved *ZT* (0.6–0.7 at 1000–1100 K) of $SrTiO_3$-based ceramic by the nano-scale modulation doping of Nb and La.

However, despite the fact that great improvements have been achieved in oxide based thermoelectric materials, the *ZT* of oxides are not sufficiently high for the minimum requirement (*ZT* > 1): $Ca_3Co_4O_9$ (0.15−0.5 at 1000 K), $Na_xCoO_2$ (0.3−0.9 at 950 K), $SrTiO_3$ (0.2−0.6 at 1000 K), $CaMnO_3$ (0.1−0.2 at 1000 K), and ZnO (0.03−0.5 at 1073 K).

### 1.3. Two dimensional electron system (2DES) in oxides

In 1993, a new perspective was introduced from the theoretical field. Hicks and Dresselhaus predicted dramatical enhancements in *ZT* in two-dimensional electron systems (2DES). In semiconductors, 2DES can be realized by quantum well structures in superlattices, and the quantum well structures significantly increase the magnitude of *S* value due to an increase in the density of states (DOS) near the conduction band edge.[56-58] This model is based on the assumption that the carrier electrons confined in such a narrow space will not experience reductions in the electrical carrier mobility/conductivity.

The 2D confinement threshold for the electrons is related to the de Broglie wavelength, $\lambda_D$, given by:

$$\lambda_D = \sqrt{\frac{2\pi\hbar^2}{k_B T m^*}}$$

where $\hbar$, $m^*$ and $k_B$ are reduced Planck's constant, effective mass of conductive carriers, and Boltzmann constant, respectively. The 2DES enhancement can be realized when the size of the quantum well is far below $\lambda_D$. The DOS near the bottom/top of the conduction/valence band increases with decreasing the quantum well thickness. This phenomenon is called the "Quantum size effect".

Following this scenario, many researches were devoted to experimentally realizing the 2DES effect, which include $Bi_2Te_3/Sb_2Te_3$ superlattice[9] and $PbTe/Pb_{0.927}Eu_{0.073}$ multiple-quantum-well[56]. Some enhanced thermoelecric performances were reported, but the effectiveness of 2D enhancement effect remained debatable as the enhancements were not as drastic as the theoretical prediction. In 2007, Ohta *et al*. used high quality $SrTi_{0.8}Nb_{0.2}O_3/SrTiO_3$ superlattice to observe a *ZT* (300K) of ~2.4 in 2DES[59]. They also have partially clarified the effectiveness of 2DES in $SrTiO_3$ using superlattices [59-61], $TiO_2/SrTiO_3$ heterointerfaces [59], and field effect transistor structures [62-64].

However, as shown in **Fig. 1**, in order to confine 2DES into highly conductive Nb-doped $SrTiO_3$ ($SrTi_{0.8}Nb_{0.2}O_3$, $n_e = 2.4 \times 10^{21}$ $cm^{-3}$) regine, very thick insullating $SrTiO_3$ layers ($n_e < 10^{15}$ $cm^{-3}$) were required. For this reason, although the enhancement of *ZT* in 2DES was significant, when the insulating layers were taken into considerations, the average *ZT* was calculated to be only ~0.24 for the whole superlattice [59]. Therefore, in order to confirm the feasibility of utilizing the 2D enhancement in practical thermoelectric applications, stronger experimental evidences are necessary.

In 2016, Dresselhaus and Saito *et al*. proposed that the PF can be dramatically improved by minimizing the quantum well thickness / $\lambda_D$ ratio in a 2D quantum well system.[58] Thus, we hypothesized that the use of longer $\lambda_D$ should be effective if the carrier electrons are confined

within a fixed layer thickness (**Fig. 2**). In this review, we summarized two systematic researches which clarified this hypothesis and confirmed the effectiveness of 2DES systems in enhancing thermoelectric performance.[65, 66]

## 2. Electron sandwich doubles the thermoelectric power factor of $SrTiO_3$

### 2.1. de Broglie wavelength of $SrTiO_3$-$SrNbO_3$ solid solution system

In order to build an effective 2DES structure for enhancing thermoelectric performances, we need to find materials with long $\lambda_D$. Our targeting material was $SrTiO_3$–$SrNbO_3$ solid solution system.[65] As Nb is doped into $SrTiO_3$ lattice, one $Ti^{4+}$ ion will be substituted by one $Nb^{5+}$ ion, generating one electron. This is a traditional electron doping method in $SrTiO_3$. However, due to the low solubility limit of $Nb^{5+}$ in $SrTiO_3$, the state-of-art bulk single crystals available are confined within the low doping range (≤ 10 mol%). Therefore, instead of using bulk crystals, we successfully fabricated $SrTiO_3$–$SrNbO_3$ full range solid solution epitaxial films on (001) $LaAlO_3$ (pseudo-cubic perovskite, lattice parameter, $a$ = 3.79 Å) substrate by pulsed laser deposition (PLD). As shown in **Fig. 3**, with Nb doping, two possible types of valence state change in the Ti and Nb ions was proposed in $SrTi_{1-x}Nb_xO_3$ ($0 < x < 1$): (1) isovalent substitution (**Fig. 3a**), where the mole fraction of $Ti^{4+}$ proportionally decreases with increasing $Nb^{4+}$ concentration ($x$); (2) heterovalent substitution (**Fig. 3b**), where two $Ti^{4+}$ or $Nb^{4+}$ ions are substituted by adjacent ($Ti^{3+}$/$Nb^{5+}$) ions. To clarify the substitution mechanism, X-ray reciprocal space mappings (RSMs) were measured to confirm the lattice constant changes, from which the valence state change of Ti and Nb ions in the $SrTi_{1-x}Nb_xO_3$ could be deduced.

The RSM measurements were performed around the (-103) diffraction spot of $LaAlO_3$ (**Fig. 4a**). All samples were incoherently grown while maintaining a cubic lattice except for samples at $x$ = 0.4 and 0.5, where slight tetragonal distortions were detected ($c/a$ = 1.0057 and

1.0050). In **Fig. 4b**, the avarage lattice parameter of the $SrTi_{1-x}Nb_xO_3$ films were plotted as a function of *x*. An M-shaped increasing trend was observed. Then, the average ionic radii in the crystal structure were calculated along with Shannon's ionic radii[67] for comparison: $Ti^{4+}$ (60.5 pm), $Ti^{3+}$ (67.0 pm), $Nb^{4+}$ (68.0 pm), and $Nb^{5+}$ (64.0 pm). For samples in $0.05 \leq x \leq 0.3$ and $x \geq 0.6$, the observed lattice parameters closely followed the heterovalent substitution line indicating that two $Ti^{4+}$ or $Nb^{4+}$ ions are substituted by adjacent ($Ti^{3+}$/ $Nb^{5+}$) ions. On the contrary, at $x = 0.4$ and 0.5, the lattice parameters were tending to comply with the isovalent substitution line. At $x = 0.5$, the B-site occupation of [$Ti^{4+}$/$Nb^{4+}$] was almost 100 % (**Fig. 4c**), which was also confirmed by the electron energy loss spectroscopy of Ti 3d *L* edge and O *K* edge.[68]

The room temperature Hall measurement for all samples was performed to obtain $\sigma$, *n*, and $\mu_{Hall}$. The general increasing tendency in $\sigma$ is mainly attributed to the increase *n* with Nb doping (**Fig. 5a and b**). But a sharp jump in $\sigma$ at $0.5 < x < 0.6$ was observed, indicating an electronic phase boundary at $x \sim 0.5$. This phenomenon is attributed to the special behavior in $\mu_{Hall}$. As shown in **Fig. 5c**, for $x < 0.5$, $\mu_{Hall}$ stay constant at ~6 $cm^2\ V^{-1}\ s^{-1}$, which is similar with previous reports.[69, 70] However, once *x* reaches 0.5, an obvious jump from ~5 $cm^2\ V^{-1}\ s^{-1}$ to ~10 $cm^2\ V^{-1}\ s^{-1}$ was observed in $\mu_{Hall}$, and as *x* further increased to 1, $\mu_{Hall}$ steadily increased to ~12 $cm^2\ V^{-1}\ s^{-1}$. Therefore, there is an electronic phase boundary at $x \sim 0.5$, which significantly changes the electric charge transport properties.

*S* is a good factor to further reveal the electronic phase boundary since it is proportional to the DOS near the Fermi level, and therefore insensitive to crystal quality. Using the measured *S* and *n*, the $m^*$ was calculated and plotted against *x* in **Fig. 5e**.[71] $m^*$ for compositions with $x <$ 0.3 was calculated to be ~1.1 $m_0$, which further decreased to ~0.7 $m_0$ as $x > 0.3$. A step-like

decease was detected at $x$ ~0.3. The step-like decrease behavior in $m^*$ at $x$ ~0.3 is attributed to the conduction band transition from Ti 3d to Nb 4d. In the relaxation time ($\tau$) changing pattern, which was extracted from $\mu_{\mathbf{Hall}} = e \cdot \tau \cdot m^{*-1}$, all samples show a constant $\tau$ around 3.5−4 fs (**Fig. 5f**) except for a sharp decrease from $x$ = 0.3 to $x$ = 0.5. This reveals the electronic phase boundary more clearly. We believe that the trough-shape trend of $\tau$ to the slight tetragonal distortion observed in the $x$ = 0.4 and 0.5 films, which could greatly increase the electron scattering cross sections[72].

According to the electrical transport property measurements, there are two types of conduction bands in $SrTi_{1-x}Nb_xO_3$ solid solutions (Ti 3d → Nb 4d), which results in large discrepancies in $m^*$ and $\lambda_D$ due to differences in the overlapping of Ti 3d orbitals from that of Nb 4d orbitals ($r_{Ti3d}$ is 48.9 pm and $r_{Nb4d}$ is 74.7 pm)[67]. These suggest that the phase diagram of $SrTi_{1-x}Nb_xO_3$ can be divided into two regions **(Fig. 6)**: Region A ($x$ < 0.3) and Region B ($x$ > 0.3). As $x$ increases $\lambda_D$ also increases from ~4.1 nm in Region A to ~5.3 nm in Region B. $\lambda_D$ is ~30 % longer in Region B. Therefore, given the confinement thicknesses are the same, it is speculated that *S*-enhancement factor in Region B is much higher than that in Region A because of the higher two-dimensionality. This makes $SrTi_{1-x}Nb_xO_3$ solid solution an ideal system to confirm the 2D enhancements effect in thermoelectric materials.

### 2.2. Double enhancement of thermoelectric power factor in the $SrTiO_3$-based superlattices

In the second research, we fabricated $SrTiO_3$-based artificial superlattices composed of [$N$ uc $SrTi_{1-x}Nb_xO_3$ | 11 uc $SrTiO_3$]$_{10}$ ($N$ = 1−12, $x$ = 0.2, 0.3, and 0.8) on (001) $LaAlO_3$ by PLD. **Figure 7** shows the Cs-corrected high-angle annular dark-field scanning transmission electron micrographs (HAADF-STEM) of the $SrTiO_3$-based artificial superlattices ($N$ = 1, $x$ = 0.6). In

the high-resolution image, the 4$^{th}$ atom in the *B*-site column shows a different contrast compared with the adjacent atoms, which indicates the existence of Nb at the 4$^{th}$ *B*-site. Similar information is also obtained in the electron energy loss spectroscopy (EELS), where the signal from the 4$^{th}$ atom is broader than that of it neighbours (**Fig. 7a**), indicating a coexistence of $Ti^{4+}/Ti^{3+}$[73] in the $SrTi_{0.4}Nb_{0.6}O_3$ layer. Furthermore, the electronic band structure of the [1 uc $SrNbO_3$|10 uc $SrTiO_3$] superlattice was calculated by the projector-augmented wave (PAW) method to confirm the 2DES formation (**Fig. 7b**). In addition to the high electron density in the 1 uc $SrNbO_3$ layer (Nb), we observed an exudation of electrons to the first and second nearest neighbored (NN) $SrTiO_3$ layers (Ti first NN and Ti second NN), where $E_F$ is located over the conduction band minimum. Although the electron diffusion cannot be removed, the diffusion of Nb could be effectively suppressed.[74] Therefore, the 2DES could mainly be confined into a 1 uc $SrTi_{1-x}Nb_xO_3$ layer and is expected to exhibit enhanced *S*.

The cross-plane $\kappa$ was measured to be ~3.3 W m$^{-1}$ K$^{-1}$ by the time-domain thermoreflectance (TDTR) method. This value is similar to the minimum limit of $CaTiO_3/SrTiO_3$-based superlattices ($\kappa$ ~3.2 W m$^{-1}$ K$^{-1}$) reported by Ravichandran *et al*.[75] In superlattice structures, phonon transport along the cross-plane direction could be significantly reduced by the interface scatterings. In this research, the low cross-plane $\kappa$ indicates that solid interfaces were formed in our superlattice structures. Based on the direct observations and indirect measurements, our [*N* uc $SrTi_{1-x}Nb_xO_3$|11 uc $SrTiO_3$]$_{10}$ superlattices (*N* is ranging from 1 to 12, *x* is ranging from 0.2 to 0.9) are appropriate to clarify the effectiveness of 2DES for enhancing PF. Note that the *ZT* cannot be calculated using the observed cross-plane $\kappa$ because the measurement direction is different from the PF measurement direction (in the in-plane direction).

The *S* and *n* of the $SrTiO_3$-based superlattices were measured at room temperature (**Fig. 8a**). It should be noted that the *n* values were calculated using the total thickness of the superlattices including the insulating $SrTiO_3$ layers. The slope of *S*–(log *n*) plot is −200 μV $K^{-1}$ $decade^{-1}$ in case of bulk systems, but our superlattices exhibit ~ −550 μV $K^{-1}$ $decade^{-1}$ for $x = 0.2$, ~ −350 μV $K^{-1}$ $decade^{-1}$ for $x = 0.3$, and ~ −250 μV $K^{-1}$ $decade^{-1}$ for $x = 0.8$. The $N = 1$ samples show largely enhanced *S* (−540 μV $K^{-1}$ for $x$=0.2, −340 μV $K^{-1}$ for $x = 0.3$, and −180 μV $K^{-1}$ for $x = 0.8$) compared with the bulk values (−143 μV $K^{-1}$ for $x = 0.2$, −73 μV $K^{-1}$ for $x = 0.3$, and −19 μV $K^{-1}$ for $x = 0.8$).

The *S*-enhancement factors, ($S_{2DES}/S_{Bulk}$) which reflects the two-dimensionality of the 2DES, were calculated and plotted against the *N* values (**Fig. 8b**). The highest $S_{2DES}/S_{Bulk}$ values for $x = 0.8$ 2DES could reach 10, two times larger than the 4 and 5 for 2DESs at $x = 0.2$ and 0.3. As hypothesized, increasing $\lambda_D$ also enhances $S_{2DES}/S_{Bulk}$. In this experiment, $S_{2DES}/S_{Bulk}$ for the $x = 0.2$ and 0.3 2DESs saturate at ~11 uc, consistent with $\lambda_D$ in Region A (~4.2 nm). Following the increased $\lambda_D$ of Region B, saturation thickness of 2DES at $x = 0.8$ shifts to much larger values, consistent with our hypothesis. These results experimentally prove that the two-dimensionality can be enhanced by increasing $\lambda_D$, which significantly boosts the thermoelectric PF.

Based on these results, we fabricated [1 uc $SrTi_{1-x}Nb_xO_3$|11 uc $SrTiO_3$]$_{10}$ superlattices with varying values of *x* between 0.2 and 0.9. **Figure 9** compares the *n* dependences of the room temperature thermoelectric properties of [1 uc $SrTi_{1-x}Nb_xO_3$|11 uc $SrTiO_3$]$_{10}$ superlattices with those of bulks. Similar to the bulks, in superlattice structures, $\sigma$ increases almost linearly with *n* (**Fig. 9a**). As a result, Region B, which has much higher *n* than Region A, should show superior performance in electron transports. Coresspondingly, we observed much higher $\sigma$ in 2DESs with $x \geq 0.6$ than in 2DESs with $x \leq 0.5$. Furthermore, the conduction band transition

(Ti 3d → Nb 4d), which was detected in the $SrTiO_3$-$SrNbO_3$ solid solution epitaxial films, can be also observed in the superlattices (**Fig. 9b**). When $x$ changes from ~0.5 to ~0.6, higher electron transport properties could be seen as $\mu_{Hall}$ increased from 3–5 $cm^2\ V^{-1}\ s^{-1}$ to ~6 $cm^2\ V^{-1}\ s^{-1}$.

In **Fig. 9c**, $-S$ values for superlattices are plotted against $n$, and bulk values also plotted for comparison.[65] The plot shows an obvious enhancement in $-S$ in 2DES compared with the bulks at similar $n$ values. As indicated by the solid lines, the experimental points for 2DES and bulk follow different slopes of –300 and –200 μV $K^{-1}$ per decade, respectively. The relationship between $-S$ and $n_{eff}$ can be expressed by the following equation.

$$|S| = -\frac{k_B}{e}\ln 10 \cdot A \cdot (\log n + B)$$

where $k_B$ is the Boltzmann constant, and $e$ is an electron charge. $A$ and $B$ are fitting parameters that depend on the type of materials and their electronic band structures. For bulks, ascribed to the 3D electronic band structure with a parabolic shaped DOS near $E_F$, $A$ is 1, so the slope will possess a constant value of $-k_B/e \cdot \ln 10$ (≡ −198 μV $K^{-1}$). On the other hand, the slope of 2DESs was about −300 μV $K^{-1}$ per decade, indicating a higher $A$ value of ~1.5. Therefore, it has been obviously proven the 2DESs prepared using $SrTi_{1-x}Nb_xO_3$ system are effective in enhancing $S$, regardless of the presence of insulating layers.

In this study, by using the conduction band transition and $\lambda_D$ enlargement in $SrTi_{1-x}Nb_xO_3$ system, we realized high $\sigma$ and large $S$ simultaneously. In **Fig. 9d**, the PFs of [1 uc $SrTi_{1-x}Nb_xO_3$|11 uc $SrTiO_3$]$_{10}$ superlattices ($0.2 \le x \le 0.9$) were calculated and plotted as a function $n$. The maximum room temperature PF of ~5.1 mW $m^{-1}\ K^{-2}$ was achieved at $n$ ~$8 \times 10^{20}$ $cm^{-3}$ for the superlattice with $x$ = 0.6, doulbing the highest value in their bulk counterparts.

## 3. Summary

We have reviewed our recent findings on doulbing the PF of a metal oxide, $SrTiO_3$, by increasing the two-dimensionallity of the 2DES. Based on the theoretical prediction by Dresselhaus and Saito *et al.*, we hypothesized that use of the longer $\lambda_D$ material as a quantum well layer is essential for enhancing the thermopower of superlattices. Firstly, we found that $\lambda_D$ in $SrTiO_3$−$SrNbO_3$ solid solution system depends on the conduction band characteristics. Then, we fabricated $SrTiO_3$-based superlattices and clarified our hypothesis on utilizing $\lambda_D$ to improve the thermoelectric performance of oxides. The approaches presented in this study will not only facilitate further improvement of $SrTiO_3$ based materials, but also be fruitful for other materials systems. These findings may also push developments in thermoelectric materials for both research investigations and practical applications.

## Experimental Section

*Fabrication and analyses of the $SrTiO_3$-based superlattices*

A series of superlattices with the chemical formula of $[N \text{ uc } SrTi_{1-x}Nb_xO_3 \mid 11 \text{ uc } SrTiO_3]_{10}$ ($1 \leq N \leq 12$, $x = 0.2$−$0.9$) were fabricated by a pulsed laser deposition (PLD) technique using dense ceramic disks of a $SrTiO_3$–$SrNbO_3$ mixture and a $SrTiO_3$ single crystal as the targets. The substrate was insulating (001) $LaAlO_3$ (pseudo-cubic perovskite, $a$ = 3.79 Å, The surface area: 1 cm × 1 cm). The substrate temperature was 900 °C. The oxygen pressure was ~$10^{-4}$ Pa, and the laser fluence was ~1.2 J $cm^{-2}$ $pulse^{-1}$. The growth conditions were precisely monitored. The thicknesses of different layers were monitored in-situ using the intensity oscillation of the reflection high-energy electron diffraction (RHEED) spots.

Crystallographic analyses of the resultant superlattices were performed by X-ray diffraction (XRD, Cu $K\alpha_1$, ATX-G, Rigaku Co.), atomic force microscopy (AFM, Nanocute, Hitachi Hi-Tech), and scanning transmission electron microscopy (STEM, 200 keV, JEM-ARM 200CF, JEOL Co. Ltd). TEM samples were fabricated using a cryo ion slicer (IB-09060CIS, JEOL Co. Ltd). High-angle annular dark-field (HAADF) images were taken with the detection angle of 68–280 mrad. Electron energy loss spectra (EELS) were acquired in STEM mode with the energy resolution of 0.8 eV.

*Measurements of the thermoelectric properties*

Electrical conductivity ($\sigma$), carrier concentration ($n$), and Hall mobility ($\mu_{\mathrm{Hall}}$) were measured at room temperature by a conventional d.c. four-probe method with a van der Pauw geometry. $S$ was measured at room temperature by creating a temperature difference ($\Delta T$) of ~4 K across the film using two Peltier devices. (Two small thermocouples were used to monitor the actual temperatures of each end of a superlattice.) The thermo-electromotive force ($\Delta V$) and $\Delta T$ were measured simultaneously, and the $S$-values were obtained from the slope of the $\Delta V$–$\Delta T$ plots (The correlation coefficient: >0.9999).

**Acknowledgements**

The authors would like to thank the collaborators, Profs. Bin Feng, Hiroyuki Hayashi, Yu-Miin Sheu, Isao Tanaka, and Yuichi Ikuhara. This research was supported by Grants-in-Aid for Scientific Research on Innovative Areas “Nano Informatics” (25106003, 25106005, and 25106007) from the Japan Society for the Promotion of Science (JSPS). H.O. was supported by Grants-in-Aid for Scientific Research A (17H01314) and B (26287064) from the JSPS. Y.Z. thanks to the China Scholarship Council (CSC) for a scholarship to study in Japan. A part of this work was supported in part by the Network Joint Research Center for Materials and Devices and by Dynamic Alliance for Open Innovation Bridging Human, Environment

and Materials. The authors gratefully thank Prof. Hai Jun Cho for his careful reading the manuscript.

Received: ((will be filled in by the editorial staff))

Revised: ((will be filled in by the editorial staff))

Published online: ((will be filled in by the editorial staff))

## References

[1] D. M. Rowe, *CRC Handbook of Thermoelectrics*, CRC Press, **1995**.

[2] H. J. Goldsmid, *Introduction to Thermoelectricity*, Springer, **2010**.

[3] T. J. Seebeck, *Abh. K. Akad. Wiss.* **1823**, *265*.

[4] M. Cutler, N. F. Mott, *Phys. Rev.* **1969**, *181*, 1336.

[5] R. Franz, G. Wiedemann, *Annalen der Physik* **1853**, *165*, 497-531.

[6] T. M. Tritt, M. A. Subramanian, *MRS Bull.* **2006**, *31*, 188-194.

[7] G. J. Snyder, E. S. Toberer, *Nature Mater.* **2008**, *7*, 105-114.

[8] D. Y. Chung, T. Hogan, P. Brazis, M. Rocci-Lane, C. Kannewurf, M. Bastea, C. Uher, M. G. Kanatzidis, *Science* **2000**, *287*, 1024-1027.

[9] R. Venkatasubramanian, E. Siivola, T. Colpitts, B. O'Quinn, *Nature* **2001**, *413*, 597-602.

[10] G. J. Snyder, M. Christensen, E. Nishibori, T. Caillat, B. B. Iversen, *Nature Mater.* **2004**, *3*, 458-463.

[11] K. F. Hsu, S. Loo, F. Guo, W. Chen, J. S. Dyck, C. Uher, T. Hogan, E. K. Polychroniadis, M. G. Kanatzidis, *Science* **2004**, *303*, 818-821.

[12] J. S. Rhyee, K. H. Lee, S. M. Lee, E. Cho, S. Il Kim, E. Lee, Y. S. Kwon, J. H. Shim, G. Kotliar, *Nature* **2009**, *459*, 965-968.

[13] L. D. Zhao, S. H. Lo, Y. S. Zhang, H. Sun, G. J. Tan, C. Uher, C. Wolverton, V. P. Dravid, M. G. Kanatzidis, *Nature* **2014**, *508*, 373.

[14] S. Il Kim, K. H. Lee, H. A. Mun, H. S. Kim, S. W. Hwang, J. W. Roh, D. J. Yang, W. H. Shin, X. S. Li, Y. H. Lee, G. J. Snyder, S. W. Kim, *Science* **2015**, *348*, 109-114.

[15] L. D. Zhao, G. J. Tan, S. Q. Hao, J. Q. He, Y. L. Pei, H. Chi, H. Wang, S. K. Gong, H. B. Xu, V. P. Dravid, C. Uher, G. J. Snyder, C. Wolverton, M. G. Kanatzidis, *Science* **2016**, *351*, 141-144.

[16] K. Koumoto, I. Terasaki, R. Funahashi, *MRS Bull.* **2006**, *31*, 206-210.

[17] K. Koumoto, Y. F. Wang, R. Z. Zhang, A. Kosuga, R. Funahashi, *Annu Rev Mater Res* **2010**, *40*, 363-394.

[18] K. Koumoto, R. Funahashi, E. Guilmeau, Y. Miyazaki, A. Weidenkaff, Y. F. Wang, C. L. Wan, *J. Am. Ceram. Soc.* **2013**, *96*, 1-23.

[19] C. Hogarth, *Phil. Mag.* **1949**, *40*, 273.

[20] G. Parravano, *The Journal of Chemical Physics* **1955**, *23*, 5-10.

[21] A. Hutson, *Journal of Physics and Chemistry of Solids* **1959**, *8*, 467-472.

[22] M. Arvin, *Phys. Chem. Solids* **1962**, *23*.

[23] H. Frederikse, W. Thurber, W. Hosler, *Physical Review* **1964**, *134*, A442.

[24] W. Thurber, A. Mante, *Physical Review* **1965**, *139*, A1655.

[25] J. Marley, R. Dockerty, *Physical Review* **1965**, *140*, A304.

[26] A. Young, C. Schwartz, *Journal of Physics and Chemistry of Solids* **1969**, *30*, 249-252.

[27] B. Griffiths, D. Elwell, R. Parker, *Philosophical Magazine* **1970**, *22*, 163-174.

[28] J. G. Bednorz, K. A. Müller, *Zeitschrift für Physik B Condensed Matter* **1986**, *64*, 189-193.

[29] J. Cooper, B. Alavi, L. Zhou, W. Beyermann, G. Grüner, *Phys Rev B* **1987**, *35*, 8794.

[30] J. Chen, C. McEwan, L. Wenger, E. Logothetis, *Phys Rev B* **1987**, *35*, 7124.

[31] N. Mitra, J. Trefny, B. Yarar, G. Pine, Z. Sheng, A. Hermann, *Phys Rev B* **1988**, *38*, 7064.

[32] M. Ohtaki, H. Koga, T. Tokunaga, K. Eguchi, H. Arai, *J Solid State Chem* **1995**, *120*, 105-111.

[33] M. Ohtaki, T. Tsubota, K. Eguchi, H. Arai, *J Appl Phys* **1996**, *79*, 1816-1818.

[34] I. Terasaki, Y. Sasago, K. Uchinokura, *Phys. Rev. B* **1997**, *56*, 12685-12687.

[35] A. Masset, C. Michel, A. Maignan, M. Hervieu, O. Toulemonde, F. Studer, B. Raveau, J. Hejtmanek, *Phys Rev B* **2000**, *62*, 166.

[36] R. Funahashi, I. Matsubara, H. Ikuta, T. Takeuchi, U. Mizutani, S. Sodeoka, *Japanese Journal of Applied Physics* **2000**, *39*, L1127.

[37] T. Okuda, K. Nakanishi, S. Miyasaka, Y. Tokura, *Phys Rev B* **2001**, *63*, 113104.

[38] S. Ohta, T. Nomura, H. Ohta, K. Koumoto, *J Appl Phys* **2005**, *97*, 034106.

[39] S. Ohta, T. Nomura, H. Ohta, M. Hirano, H. Hosono, K. Koumoto, *Appl Phys Lett* **2005**, *87*, 092108.

[40] Z. L. Lu, H. R. Zhang, W. Lei, D. C. Sinclair, I. M. Reaney, *Chem. Mater.* **2016**, *28*, 925-935.

[41] J. Wang, B. Y. Zhang, H. J. Kang, Y. Li, X. B. Yaer, J. F. Li, Q. Tan, S. Zhang, G. H. Fan, C. Y. Liu, L. Miao, D. Nan, T. M. Wang, L. D. Zhao, *Nano Energy* **2017**, *35*, 387-395.

[42] R. Funahashi, I. Matsubara, H. Ikuta, T. Takeuchi, U. Mizutani, S. Sodeoka, *Jpn J Appl Phys 2* **2000**, *39*, L1127-L1129.

[43] W. Koshibae, K. Tsutsui, S. Maekawa, *Phys. Rev. B* **2000**, *62*, 6869-6872.

[44] G. A. Slack, *CRC handbook of thermoelectrics* **1995**, 407-440.

[45] G. Jonker, J. Van Santen, *CrossRef Google Scholar* **1950**.

[46] E. Wollan, *Phys. Rev.* **1955**, *100*, 545.

[47] J. B. Goodenough, *Phys. Rev.* **1955**, *100*, 564.

[48] J. MacChesney, H. Williams, J. Potter, R. Sherwood, *Physical Review* **1967**, *164*, 779.

[49] Y. Wang, Y. Sui, H. J. Fan, X. J. Wang, Y. T. Su, W. H. Su, X. Y. Liu, *Chem Mater* **2009**, *21*, 4653-4660.

[50] R. Funahashi, A. Kosuga, N. Miyasou, E. Takeuchi, S. Urata, K. Lee, H. Ohta, K. Koumoto, in *Thermoelectrics, 2007. ICT 2007. 26th International Conference on*, IEEE, **2007**, pp. 124-128.

[51] K. Park, J. Seong, G. Kim, *Journal of Alloys and Compounds* **2009**, *473*, 423-427.

[52] K. Park, K. Y. Ko, *Journal of Alloys and Compounds* **2007**, *430*, 200-204.

[53] K. Park, J. Seong, *Journal of Alloys and Compounds* **2008**, *464*, 1-5.

[54] K. Park, J. Seong, S. Nahm, *Journal of Alloys and Compounds* **2008**, *455*, 331-335.

[55] L. Mattheiss, *Phys Rev B* **1972**, *6*, 4718.

[56] L. D. Hicks, T. C. Harman, X. Sun, M. S. Dresselhaus, *Phys. Rev. B* **1996**, *53*, 10493-10496.

[57] L. D. Hicks, M. S. Dresselhaus, *Phys. Rev. B* **1993**, *47*, 12727-12731.

[58] N. T. Hung, E. H. Hasdeo, A. R. T. Nugraha, M. S. Dresselhaus, R. Saito, *Phys. Rev. Lett.* **2016**, *117*, 036602.

[59] H. Ohta, S. Kim, Y. Mune, T. Mizoguchi, K. Nomura, S. Ohta, T. Nomura, Y. Nakanishi, Y. Ikuhara, M. Hirano, H. Hosono, K. Koumoto, *Nature Materials* **2007**, *6*, 129-134.

[60] Y. Mune, H. Ohta, K. Koumoto, T. Mizoguchi, Y. Ikuhara, *Appl. Phys. Lett.* **2007**, *91*, 192105.

[61] K. H. Lee, Y. Mune, H. Ohta, K. Koumoto, *Appl Phys Express* **2008**, *1*, 015007.

[62] H. Ohta, Y. Masuoka, R. Asahi, T. Kato, Y. Ikuhara, K. Nomura, H. Hosono, *Appl. Phys. Lett.* **2009**, *95*, 113505.

[63] H. Ohta, Y. Sato, T. Kato, S. Kim, K. Nomura, Y. Ikuhara, H. Hosono, *Nature Commun.* **2010**, *1*.

[64] H. Ohta, T. Mizuno, S. J. Zheng, T. Kato, Y. Ikuhara, K. Abe, H. Kumomi, K. Nomura, H. Hosono, *Adv. Mater.* **2012**, *24*, 740-744.

[65] Y. Zhang, B. Feng, H. Hayashi, T. Tohei, I. Tanaka, Y. Ikuhara, H. Ohta, *J. Appl. Phys.* **2017**, *121*, 185102.

[66] Y. Q. Zhang, B. Feng, H. Hayashi, C. P. Chang, Y. M. Sheu, I. Tanaka, Y. Ikuhara, H. Ohta, *Nature Commun.* **2018**, *9*, 2224.

[67] R. D. Shannon, *Acta Crystallogr A* **1976**, *32*, 751-767.

[68] Y. Q. Zhang, B. Feng, H. Hayashi, T. Tohei, I. Tanaka, Y. Ikuhara, H. Ohta, *J. Appl. Phys.* **2017**, *121*.

[69] H. P. R. Frederikse, W. R. Thurber, W. R. Hosler, *Phys. Rev.* **1964**, *134*, A442.

[70] O. N. Tufte, P. W. Chapman, *Phys. Rev.* **1967**, *155*, 796.

[71] C. B. Vining, *J Appl Phys* **1991**, *69*, 331-341.

[72] M. Yamamoto, H. Ohta, K. Koumoto, *Appl. Phys. Lett.* **2007**, *90*, 072101.

[73] A. Ohtomo, D. A. Muller, J. L. Grazul, H. Y. Hwang, *Nature* **2002**, *419*, 378-380.

[74] T. Mizoguchi, H. Ohta, H. S. Lee, N. Takahashi, Y. Ikuhara, *Adv. Funct. Mater.* **2011**, *21*, 2258-2263.

[75] J. Ravichandran, A. K. Yadav, R. Cheaito, P. B. Rossen, A. Soukiassian, S. J. Suresha, J. C. Duda, B. M. Foley, C. H. Lee, Y. Zhu, A. W. Lichtenberger, J. E. Moore, D. A. Muller, D. G. Schlom, P. E. Hopkins, A. Majumdar, R. Ramesh, M. A. Zurbuchen, *Nature Mater.* **2014**, *13*, 168-172.

[76] D. Oka, Y. Hirose, S. Nakao, T. Fukumura, T. Hasegawa, *Phys Rev B* **2015**, *92*.

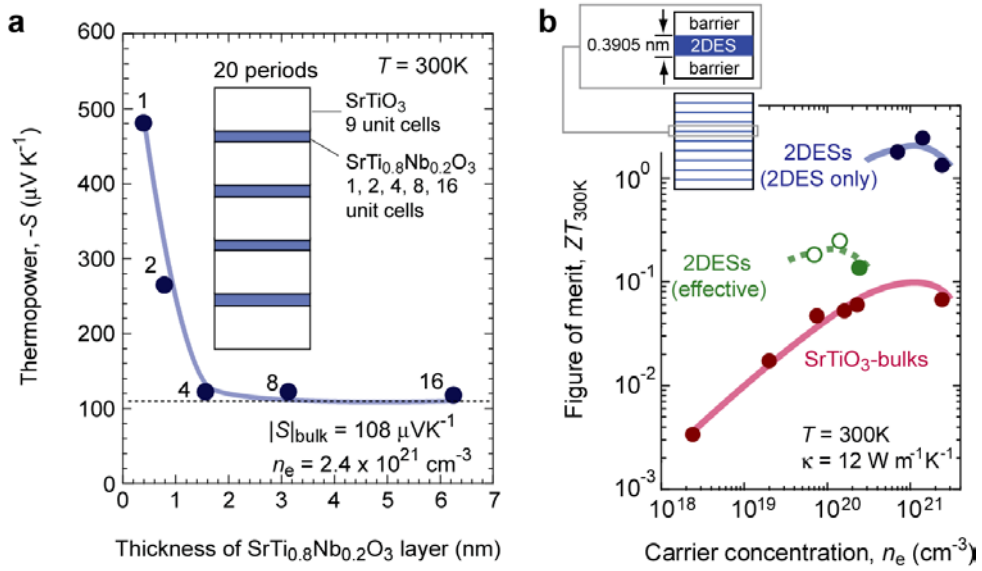


**Fig. 1 | Thermoelectric response of the 2DES confined in an MQW composed of $SrTiO_3$ (barrier)/$SrTi_{0.8}Nb_{0.2}O_3$ (well)/$SrTiO_3$ (barrier). a** $|S|_{300\ K}$ versus well thickness for the $SrTiO_3$/$SrTi_{0.8}Nb_{0.2}O_3$/$SrTiO_3$ MQWs. A dramatic increase in $|S|_{300\ K}$ is seen when the thickness of the $SrTi_{0.8}Nb_{0.2}O_3$ layer is smaller than 1.56 nm (four unit cells of $SrTiO_3$). **b** *ZT* value of the 2DESs and the $SrTiO_3$-bulk samples as a function of carrier concentration at room temperature. Inset: Schematic illustration of the MQW structure composed of nine unit cells of barrier layer and one unit cell 2DES layer. The electrical conductivity ($\sigma_{300\ K}$) was estimated using observed $n_e$ together with the carrier mobility of $SrTiO_3$, $\mu_{300\ K}$ of 6 $cm^2\ V^{-1}\ s^{-1}$. The *ZT* values were estimated using the values of $\sigma$, $|S|$ and the bulk $\kappa$ for $SrTiO_3$ (12 $Wm^{-1}\ K^{-1}$) at 300 K. Effective *ZT* for the MQW sample (3) is plotted (green filled circle), whereas that of the other 2DES samples (1, 2) is estimated (open circles) as $ZT_{eff.} = ZT_{2DES}/(1+ N_{barrier})$, where $N_{barrier}$ is 9, the number of unit cells of the $SrTiO_3$ barrier layer. The lines are guides for the eyes. Reproduced with permission.[59] Copyright 2007, Springer Nature.

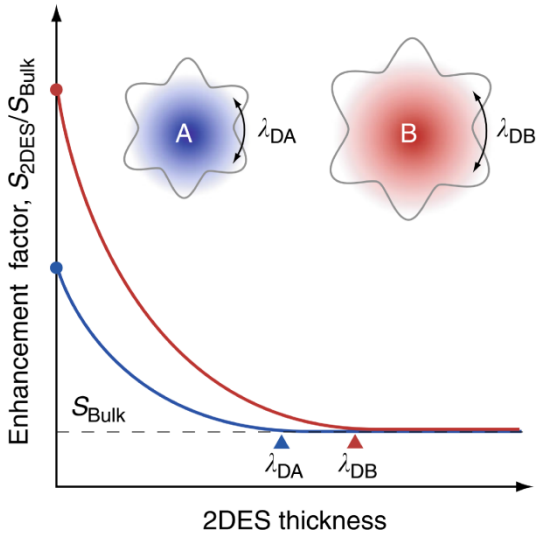


**Fig. 2 | Hypothesis of thermoelectric effect of a two-dimensional electron system.** It is hypothesized that a 2DES with longer de Broglie wavelength ($\lambda_D$) shows a larger enhancement factor of thermopower. Reproduced with permission.[66] Copyright 2018, Springer Nature.

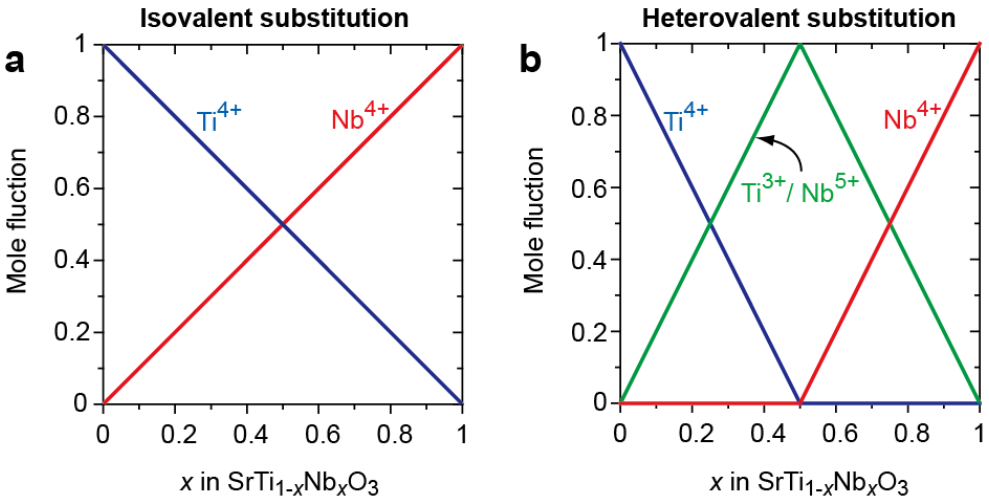


**Fig. 3 | Possible valence state changes in the $SrTiO_3$–$SrNbO_3$ solid solution system. a** isovalent substitution, where $Ti^{4+}$ is substituted by $Nb^{4+}$; **b** heterovalent substitution, where two $Ti^{4+}$/$Nb^{4+}$ ions are substituted by adjacent $Ti^{3+}$/$Nb^{5+}$ ions. Reproduced with permission.[65] Copyright 2017, American Institute of Physics.

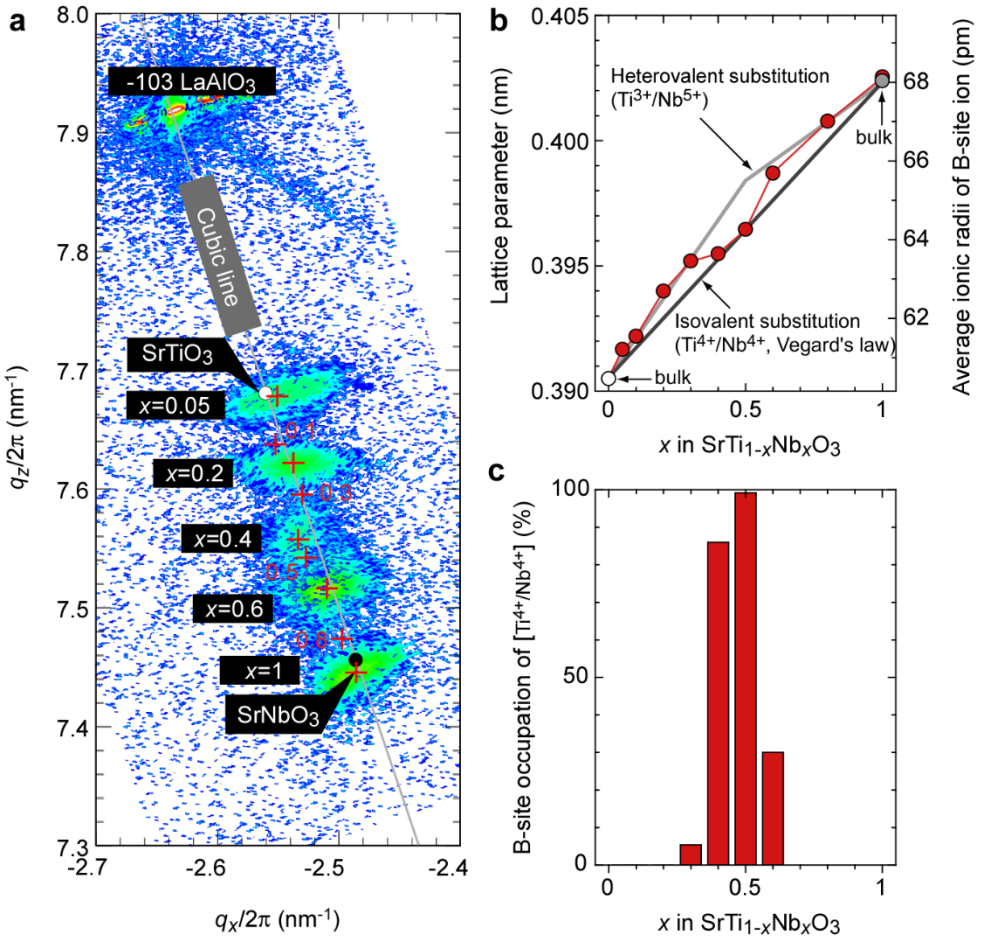


**Fig. 4 | Crystallographic characterization of the $SrTi_{1-x}Nb_xO_3$ epitaxial films on a (001) $LaAlO_3$ single crystal substrate. a** X-ray reciprocal space mappings around the (−103) diffraction spot of the $SrTi_{1-x}Nb_xO_3$ epitaxial films. The location of the $LaAlO_3$ diffraction spot, $(q_x/2\pi, q_z/2\pi) = (-2.64, 7.92)$, corresponds with the pseudo-cubic lattice parameter of $LaAlO_3$ ($a$ = 3.79 Å). Red symbols (+) indicate the peak positions of the $SrTi_{1-x}Nb_xO_3$ epitaxial films. **b** Changes in the lattice parameters of the $SrTi_{1-x}Nb_xO_3$ films (circles, left axis), with superimposed isovalent/heterovalent substitution lines (black line: isovalent substitution, gray line: heterovalent substitution, right axis), calculated using Shannon's ionic radii.[67] **c** Change in the B-site occupation by $[Ti^{4+}/Nb^{4+}]$ derived from the data in **b**. Reproduced with permission. [65] Copyright 2017, American Institute of Physics.

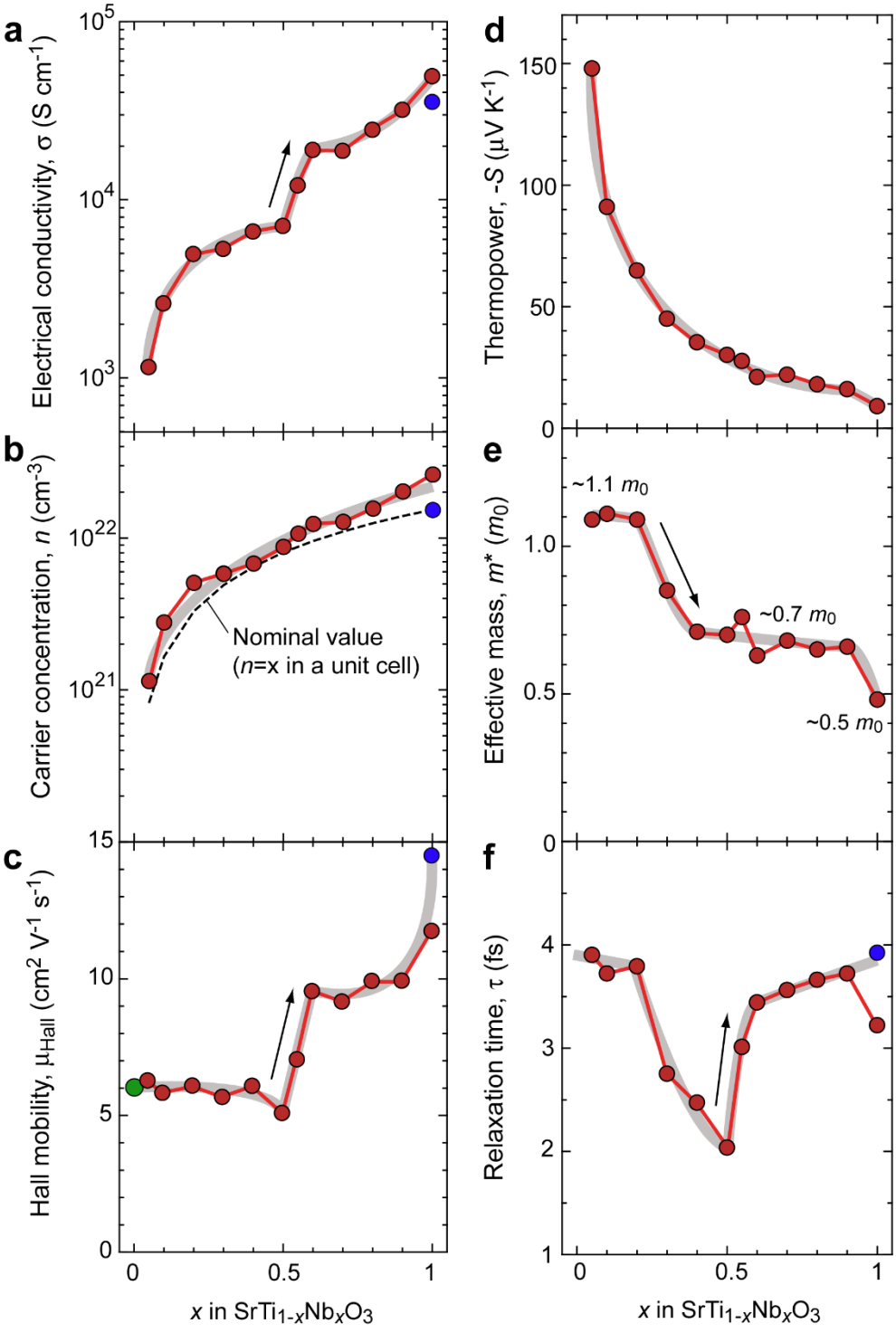


**Fig. 5 | Room temperature electron transport properties of the $SrTi_{1-x}Nb_xO_3$ epitaxial films. a** electrical conductivity ($\sigma$), **b** carrier concentration ($n$), **c** Hall mobility ($\mu_{Hall}$), **d** thermopower ($S$), **e** effective mass ($m^*$), and **f** carrier relaxation time ($\tau$). Previously reported data for $\sigma$, $n$, and $\mu_{Hall}$ are plotted for comparison (blue circles indicate the $SrNbO_3$ film from Ref. [76]; green circles are for slightly Nb-doped $SrTiO_3$ [69]). The gray lines are drawn as a guide. Reproduced with permission. [65] Copyright 2017, American Institute of Physics.

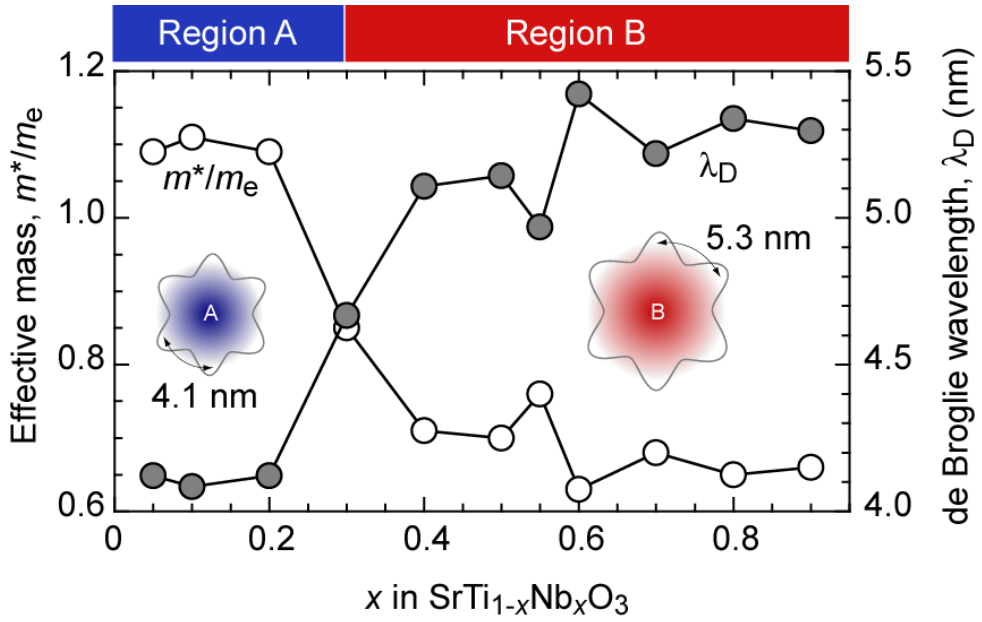


**Fig. 6 | $SrTiO_3$–$SrNbO_3$ solid solution: a model system having two different $\lambda_D$.** *x*-dependent effective mass ($m^*/m_e$, white symbols) and $\lambda_D$ (gray symbols) for $SrTi_{1-x}Nb_xO_3$ solid solutions. $m^*/m_e$ exerts a decreasing tendency with *x*, resulting in an increased $\lambda_D$. Sharp changes in both $m^*/m_e$ and $\lambda_D$ are detected around $x = 0.3$ due to the conduction band transition from Ti 3d to Nb 4d. The properties of $SrTi_{1-x}Nb_xO_3$ solid solutions can be divided into two regions based on the conduction bands (Ti 3d → region A and Nb 4d → region B). Inset: schematic illustrations of conduction electrons at regions A and B. At region B, $\lambda_D$ is ~5.3 nm, while it is ~4.1 nm at region A. Reproduced with permission. [66] Copyright 2018, Springer Nature.

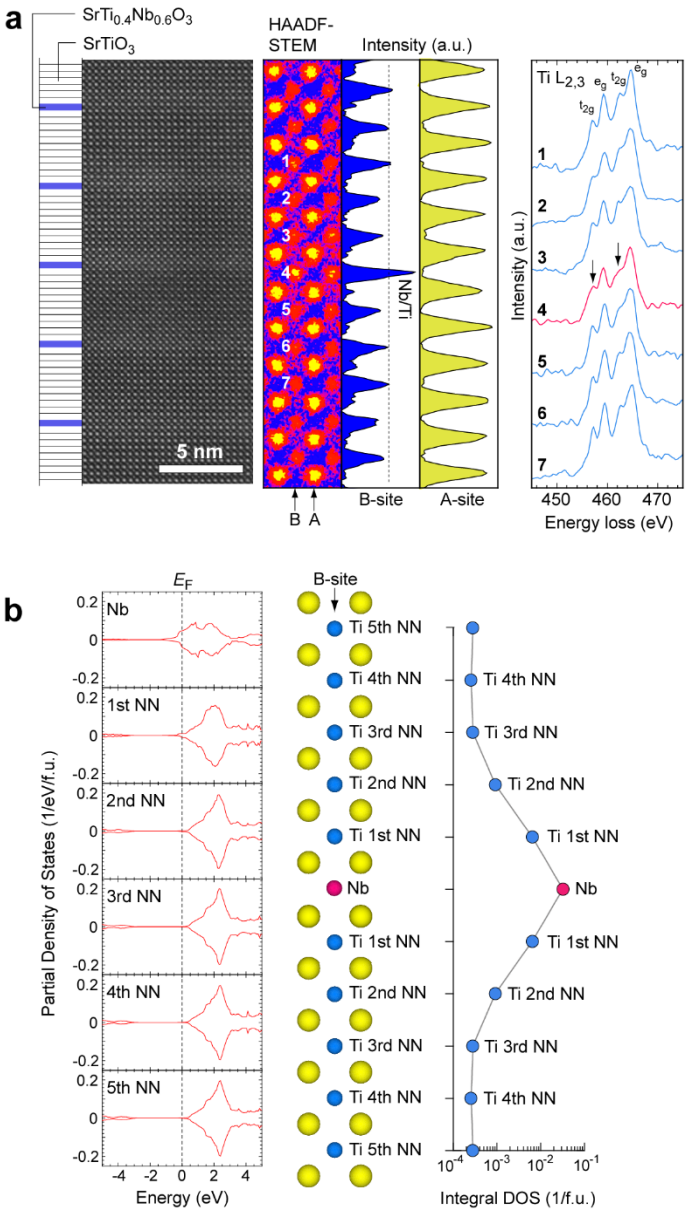


**Fig. 7 | Experimental and theoretical analyses of the 2DES. a** Cross-sectional HAADF-STEM image of the [1 uc $SrTi_{0.4}Nb_{0.6}O_3$|11 uc $SrTiO_3$]$_{10}$ superlattice. Layer stacking sequence is also shown. Rather bright bands are seen near each $SrTi_{0.4}Nb_{0.6}O_3$ layer. In the magnified image, the #4 atom in the B-site column is brighter than the nearby atoms, whereas no obvious difference is observed in the A-site column. EELS spectrum of #4 is broader than that of nearby atoms, indicating the coexistence of $Ti^{4+}/Ti^{3+}$ in the $SrTi_{0.4}Nb_{0.6}O_3$ layers. **b** The calculated partial DOS of Nb 4d or Ti 3d in the [1 uc $SrNbO_3$|10 uc $SrTiO_3$] superlattice. The Fermi energy ($E_F$) is located on the higher-energy side of the conduction band minimum for the first and second nearest neighbor (Ti first NN and Ti second NN). $SrTiO_3$ layers together with 1 uc $SrNbO_3$ layer (Nb) suggest that the electron carriers can seep from the $SrTi_{1-x}Nb_xO_3$ layers into the $SrTiO_3$ layers. Reproduced with permission. [66] Copyright 2018, Springer Nature.

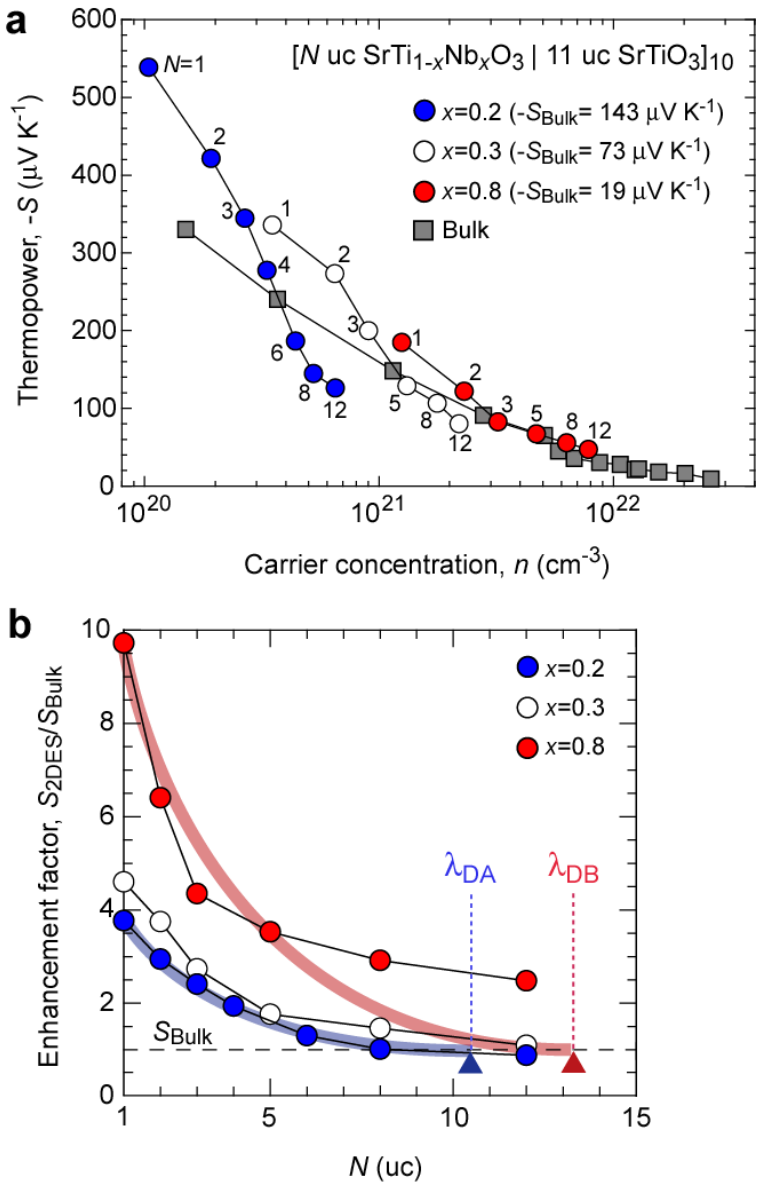


**Fig. 8 | Two-dimensionality of 2DES: a key to enhance thermopower. a** Plots of thermopower of the 2DESs, [*N* uc $SrTi_{1-x}Nb_xO_3$|11 uc $SrTiO_3$]$_{10}$ superlattices ($x$ = 0.2, 0.3, and 0.8), versus the carrier concentration ($n$). Compared to bulk values (gray squares), all the 2DESs show an enhanced $-S$ as $N$ is reduced under 3 uc. **b** Enhancement factors in $-S$ ($S_{2DES}/S_{Bulk}$) for three sets of 2DESs. For $x$ = 0.2 and 0.3 2DESs, the highest $S_{2DES}/S_{Bulk}$ values are obtained at $N$ = 1, which are 4 and 5, respectively, while that of $x$ = 0.8 can reach 10. Reproduced with permission. [66] Copyright 2018, Springer Nature.

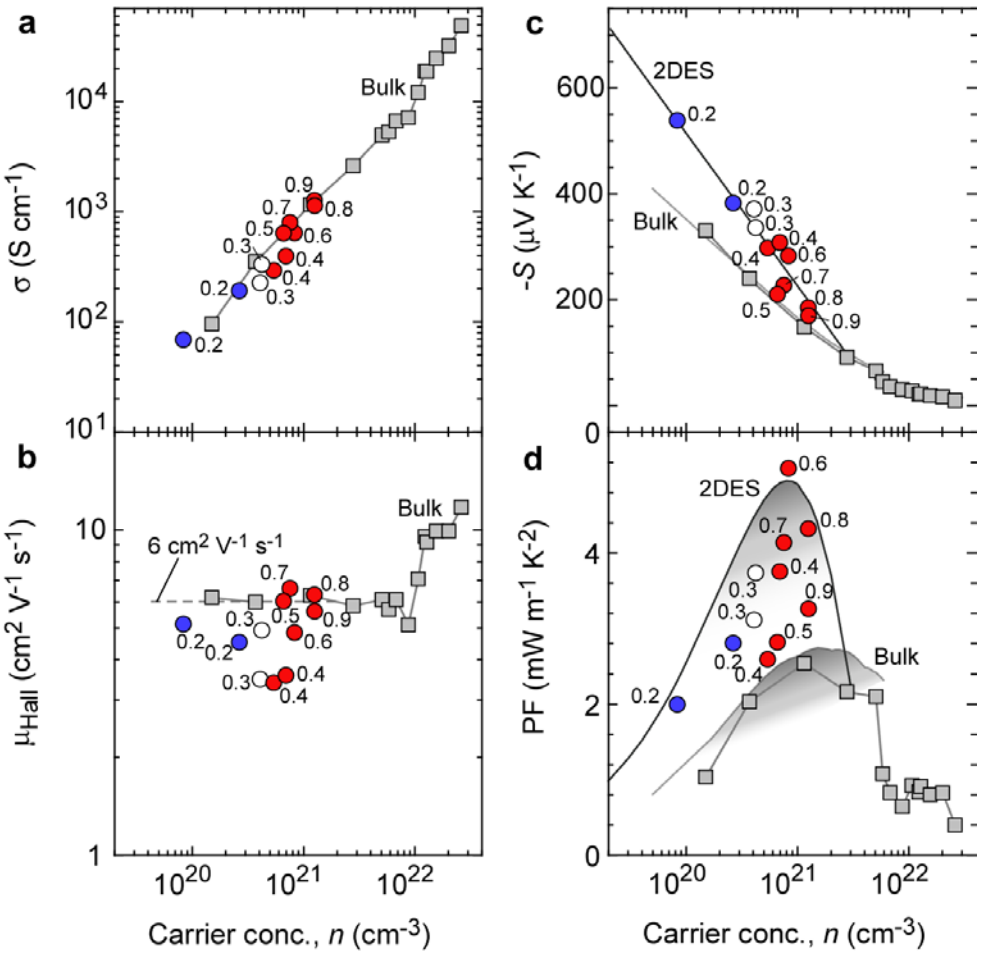


**Fig. 9 | Double enhancement of the thermoelectric PF in a 2DES.** Carrier concentration dependences of **a** electrical conductivity ($\sigma$), **b** Hall mobility ($\mu_{Hall}$), **c** thermopower ($-S$), and **d** PF of [1 uc $SrTi_{1-x}Nb_xO_3$| 11 uc $SrTiO_3$]$_{10}$ 2DESs ($x$ is ranging from 0.2 to 0.9) at room temperature. Similar to the trends in the bulk values, $\sigma$ increases almost linearly with $n$. $\mu_{Hall}$ for lower $x$ samples ($x \leq 0.5$) fluctuates around 3–5 cm$^2$ V$^{-1}$ s$^{-1}$, while that for higher $x$ ones ($x \geq 0.6$) is ~6 cm$^2$ V$^{-1}$ s$^{-1}$. Slope of $-S$ versus log$n$ for bulk $SrTi_{1-x}Nb_xO_3$ is –198 μV K$^{-1}$, which is ~1.5 times lower than –300 μVK$^{-1}$ for the 2DESs. Double enhancement of PF is seen in $x$=0.6 (5.1 mW m$^{-1}$ K$^{-2}$ at $n$~8 × 10$^{20}$ cm$^{-3}$). Since the PF values are scattered due to the rather large distribution of $\mu_{Hall}$ (3–6 cm$^2$ V$^{-1}$ s$^{-1}$), we calculated PFs using the relationship between $S$ and $n$ at constant $\mu_{Hall}$ (6 cm$^2$ V$^{-1}$ s$^{-1}$). The optimized PF of the 2DES should be ~5 mW m$^{-1}$ K$^{-2}$ at $n$~8 × 10$^{20}$ cm$^{-3}$, which doubles that of bulk $SrTi_{1-x}Nb_xO_3$ (PF ~2.5 mW m$^{-1}$ K$^{-2}$ at $n$ ~2×10$^{21}$ cm$^{-3}$). Reproduced with permission. [66] Copyright 2018, Springer Nature.

**Yuqiao Zhang**

Yuqiao Zhang is a Ph.D. candidate in the Graduate School of Information Science and Technology at Hokkaido University, Japan. He received B.S. from University of Jinan, China in 2012 and M.S. from University of Science and Technology Beijing, China in 2015. And in the same year, he joined Prof. Hiromichi Ohta's group as a Ph.D. candidate. His main research interests focus on the fabrication and electron/phonon transport clarifications of $SrTiO_3$ based thermoelectric materials, including $SrTiO_3$–$SrNbO_3$ epitaxial films and superlattices.

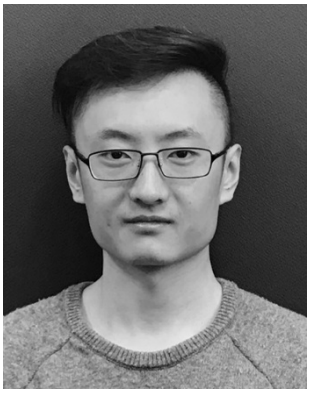

**Hiromichi Ohta, Ph.D.**

Dr. Ohta is currently Professor of Research Institute for Electronic Science at Hokkaido University, Japan. He received B.S. from Saitama University in 1994, M.S. from Nagoya University in 1996, and Ph.D. from Tokyo Institute of Technology in 2001. He worked at two companies, SANYO Electric (Li-ion battery) and HOYA (transparent conducting oxide including $InGaZnO_4$). In 1999, he joined to Prof. Hosono's Project, ERATO, JST (Transparent oxide semiconductors). In 2003, he moved to Nagoya University as an Associate Professor and worked on thermoelectric oxides, especially 2DES in $SrTiO_3$. In 2012, he moved to Hokkaido University.

**Electron sandwich, the carrier electrons confined within one atomic layer of oxide crystal between two insulating oxides,** doubled the thermoelectric power factor, the ability of a material to convert heat into electricity. This finding could help reduce the amount of wasted heat and thus wasted fossil fuel, in daily activities and industries.

**Keyword**

thermoelectric power factor, de Broglie wavelength, superlattice, two-dimensionality, $SrTiO_3$−$SrNbO_3$ solid-solution

Y. Zhang and H. Ohta*

**Electron sandwich doubles the thermoelectric power factor of $SrTiO_3$**